Energy & Environmental Science

ROYAL SOCIETY OF CHEMISTRY

PAPER

View Article Online
View Journal

Cite this: DOI: 10.1039/d2ee04137e

Translucent perovskite photovoltaics for building integration†

D. B. Ritzer, *[ab] B. Abdollahi Nejand, [ab] M. A. Ruiz-Preciado, [ab] S. Gharibzadeh,[b] H. Hu,[ab] A. Diercks,[b] T. Feeney,[b] B. S. Richards, [ab] T. Abzieher‡[b] and U. W. Paetzold *[ab]

Received 23rd December 2022,
Accepted 4th April 2023

DOI: 10.1039/d2ee04137e

rsc.li/ees

Transparent photovoltaics provide diverse levels of average visible transmittance (AVT) along with concurrent light harvesting, making glass façades and windows accessible for photovoltaics. However, improvements in power conversion efficiency (PCE) and aesthetics are required to enhance commercial viability and public acceptance. This work presents the scalable fabrication of efficient micro-patterned translucent perovskite photovoltaics at optical qualities suited for building integration. Optimized laser-scribed transparent areas (25 μm) mitigate detrimental effects on electrical performance, featuring perovskite solar cells with 44% AVT and demonstrating industrial glass quality through neutral color rendering (CRI 97) and only 3% haze. Highlighting scalability, submodules yield PCEs of 9.0% at 32% AVT (4 cm^2 aperture area). The transfer to two-terminal perovskite–perovskite tandem solar cells exhibiting PCEs of 17.7% at 12% AVT and 11.1% at 31% AVT demonstrates the first translucent perovskite tandem photovoltaics. Lastly, the novel concept of transmittance gradients with 7% cm^{-1} absolute change in AVT and 12.0% PCE for submodules is presented, providing a foundation for architectural individualizations.

Broader context

Driven by the transition to renewable energy technologies along with the growing competition for land, the application of building-integrated photovoltaics (PV) is crucial for an efficient use of urban space. In order to make surfaces such as façades and windows accessible as well, transparent PV technologies are required, which so far have been associated with strong coloration, heterogeneous appearance and often severely reduced efficiency. In this work, we combine thin-film perovskite-based photovoltaics, a promising PV technology due to unique optoelectronic properties, with optimized laser-induced micro-patterning of transparent areas to produce efficient solar cells with diverse levels of transparency. The resulting optical appearance is uniform and neutral color rendering achieved at industrial glass quality standards. In addition, efficient upscaling to modules, the transfer to more complex yet more efficient tandem devices and novel design concepts with variations in transparency are presented.

1. Introduction

Considering the modern competition for land, building integrated photovoltaics (BIPV) is crucial to accelerate the wide spread of photovoltaics and thereby contribute to the transition from a carbon-based energy system to innovative and cost-effective renewable energy technologies. Furthermore, the local, decentralized generation of electricity *via* BIPV implies system advantages by reducing power grid infrastructure, transmission losses as well as installation costs.[1,2] Moreover, as conventional opaque photovoltaic (PV) is hardly applicable to more than rooftops, making surfaces around buildings accessible with BIPV bears the promise to significantly increase the light harvesting per building and help to achieve net zero energy consumption.[3,4] However, facades, windows or skylights require special consideration as good daylighting autonomy is pivotal while uncomfortably high illuminance levels (*e.g.* glare) or passive solar heating shall be omitted to reduce energy consumption.[5,6] Offering both, variable average visible transmittance (AVT) and typically inversely proportional power conversion efficiency (PCE), transparent PV promise ideal

[a] *Institute of Microstructure Technology (IMT), Karlsruhe Institute of Technology (KIT), Hermann-von-Helmholtz-Platz 1, 76344 Eggenstein-Leopoldshafen, Germany. E-mail: david.ritzer@kit.edu*
[b] *Light Technology Institute (LTI), Karlsruhe Institute of Technology (KIT), Engesserstrasse 13, 76131, Karlsruhe, Germany. E-mail: ulrich.paetzold@kit.edu*

† Electronic supplementary information (ESI) available. See DOI: https://doi.org/10.1039/d2ee04137e

‡ Present address: National Renewable Energy Laboratory, Golden, CO 80401, USA.

daylighting adjusted by and in synergy with efficient energy harvesting.[2,7] Extensive research on the compositional adaption of photoactive materials,[8,9] tuning of their optoelectronic properties,[10,11] modification of layer stacks and thicknesses[12,13] and their combination with photochromic layers[14,15] led to various transparent PV technologies with a wide spread of features and benefits.[16] However, considering the large gap between so-far-achieved PCEs and the respective theoretical limit at given application-oriented AVTs, transparent PV consistently requires an improvement in fabrication processes to maximize PCEs and create economic incentives.[1,17,18] Additionally, enhancement of neutral color rendering, sharpness of view and design flexibility is pivotal in order to avoid any adverse effects that come with the substitution of conventional façade elements.[7]

Transparent PVs can be categorized into wavelength-selective and non-wavelength-selective absorption depending on whether or not light is preferentially harvested in the ultraviolet (UV) and/or near-infrared (NIR) and transmitted in the visible spectrum. Wavelength-selective transparent PVs employ organic small molecules[19,20] or polymers[21] to absorb photons *via* distinct energy transitions across the bandgap of a semiconductor or from the highest occupied molecular orbital to the lowest unoccupied molecular orbital in an organic molecule. Thereby, ultra-violet (UV) and/or near infrared (NIR) radiation is harvested while the discontinuity of states is exploited to ensure transmission of the visible spectrum. In accordance, very high AVT values of 50–90% can be achieved for this technology at mm^2 device dimensions as shown in Fig. 1, while the theoretical Shockley–Queisser limit of 20.6% PCE at 100% AVT shows its thermodynamic limit (optimal bandgap of 1.12 eV).[22,23] (Following the widely accepted definition, the AVT in this work is reported as the integration of transmission spectrum weighted against the photopic response of the human eye in the range of 380 nm to 780 nm and the illumination intensity of the solar spectrum for an air mass of 1.5 times the atmosphere's thickness (AM1.5G).[17,24]) An NIR-selective transparent PV was demonstrated in 2011 by Lunt *et al.* with 1.7% PCE at 55% AVT by combining a heterojunction organic PV, organic donor and acceptor layers with peak absorption in the UV and NIR and a NIR-wavelength-selective mirror coating.[25] Utilizing a visibly transparent polymer layer with silver nanowire as top-electrode, Chen *et al.* reported 4.0% PCE at 61% AVT in 2012.[26] An attempt to increase the PCE beyond 5% *via* a two-junction approach of Zuo *et al.* has so far led to a considerable improvement, corresponding to 10.7% PCE at 53% AVT.[27] The large gap between so-far-achieved PCEs and the theoretical limit of wavelength-selective transparent

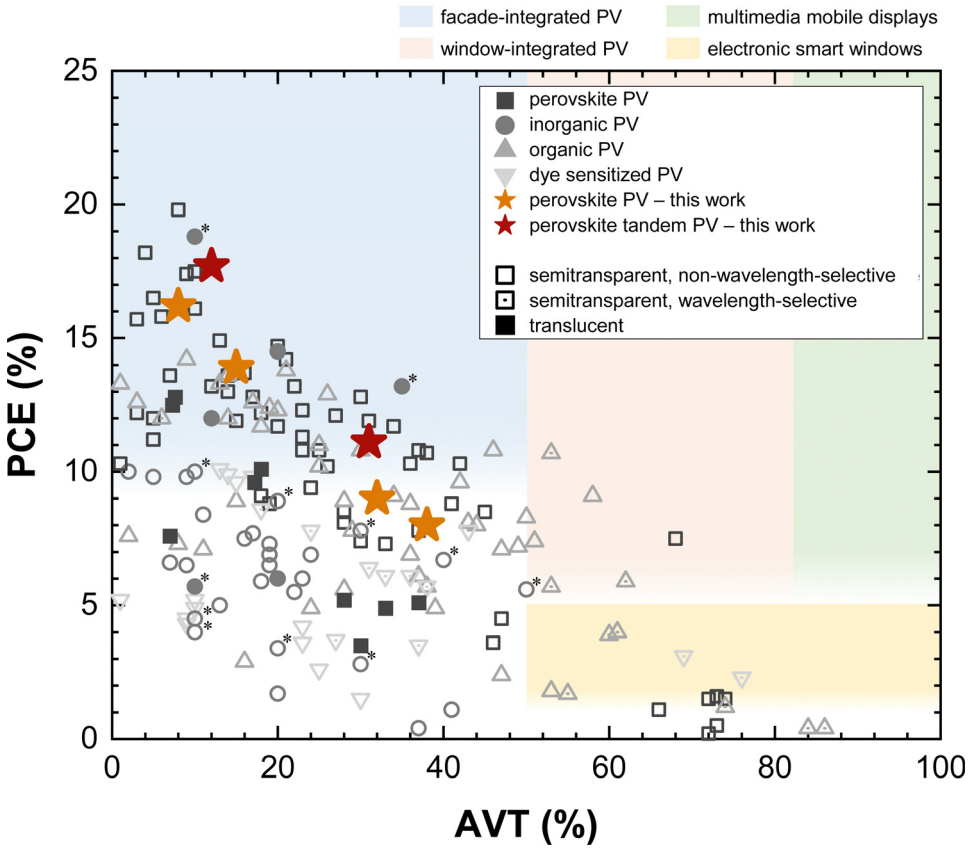

Fig. 1 Power conversion efficiencies as a function of average visible transmittance for transparent photovoltaics being based on different technological approaches. Data points marked with an asterisk (*) represent transparent photovoltaic panels available in industry and at m^2 dimensions. Detailed information about the data points is summarized in Fig. S1 and Table S1 in the ESI.† Estimated application requirements for technological and economic viability of transparent PV are depicted as colored background divisions.[17]

PVs is partly owed to the problematic exciton diffusion length that necessitates to constrain the layer thickness and thereby its absorbance. Based on the indispensable use of transparent electrode layers with generally inferior conductivity than opaque materials, upscaling transparent PVs leads to a trade-off between the reduction in AVT, the increase in series resistance losses and the requirement for a higher periodicity of interconnections, thereby reducing its active area. Transferring the approach of wavelength-selective absorption to luminescent solar concentrators (LSC), Yang *et al.* demonstrated a NIR-selective LSC based on luminophores with 1.2% PCE at 74% AVT.[28] As the reabsorption of photons is the dominant loss mechanism for LSCs when scaling towards device dimensions of square meters,[29] LSCs that exhibit UV absorption and reemission in NIR spectrum have become more attractive. The lower ratio of UV photons in the solar spectrum (AM1.5G) however limits the theoretical PCE of these devices to 5.6% (with exploitation of multiexciton generation mechanisms and a cut-off wavelength of 435 nm due to the negligible sensitivity of the human eye).[30] As a result of the very high AVTs of wavelength-selective transparent PVs, this technology is envisaged to be applied in self-powered smart windows, as shown in Fig. 1. Depending on the improvement in PCE and upscaling of device dimensions, applications as window-integrated PV or to self-power small electronic devices from multimedia mobile displays can become technically and economically viable.[17] However, its fundamental limitations in regard to PCE renders wavelength-selective transparent PVs unattractive for application in façades.

Non-wavelength-selective transparent PVs are categorized into translucent and semitransparent PV. The latter, non-wavelength-selective semitransparent PV, is based on photoactive materials that absorb in a broad wavelength range including the visible spectrum and are either thin enough or have a large enough bandgap to allow for the transmission of a fraction of the incident light. Since this technology, unlike wavelength-selective transparent PVs, absorbs extensively in the visible region for efficient energy harvesting, a direct trade-off between PCE and AVT is evident. Available for more than one decade,[31,32] commercial products are based on hydrogenated amorphous silicon (a-Si:H), copper indium gallium selenide (CIGS) or cadmium telluride (CdTe) thin-film PV, the latter two offering higher PCEs while being at a slight competitive disadvantage due to higher costs and less abundant elements.[33] Obtainable at common dimensions of $\sim$1 m^2, modern semitransparent PV panels provide up to 10% PCE at 10% AVT and 6% at 50% AVT.[34,35] Beyond these established technologies, research recently pursues the development of semitransparent devices based on emerging PV technologies like organic photovoltaics (OPV) and perovskite photovoltaics. These laboratory-scale semitransparent devices with active area dimensions of typically several mm^2 to few cm^2 yielded PCEs between 9.1% and 19.8% at AVT values of 8% to 58%.[36,37] In this regard, Yang *et al.* fabricated a semitransparent perovskite solar with 19.8% PCE at 8% AVT, exploiting a thin gold layer grown on a chromium seed layer as transparent front contact for increased transmittance.[16,36] Furthermore, Chaturvedi *et al.* recently demonstrated slot-die coated organic solar cells with PCEs of up to 9.1% at 58% AVT based on the additional deposition of Ag nanowires on Al-doped ZnO as transparent back electrode.[37] While the concept of multi-junction semitransparent PVs can further improve the theoretical PCE limit, the achievable AVT reduces significantly due to the incremental visible absorption of additional layers. Employing this approach, Meiss *et al.* presented an efficient 2-terminal tandem organic solar cell with 5.1% PCE at 24% AVT, being based on two optimized small molecule organic bulk heterojunctions.[38] Independent of the materials used, non-wavelength-selective semitransparent PVs exhibit a strong color and accordingly low color rendering indices (CRI) due to the wavelength-dependent variations in absorbance, reflectance and transmittance in the visible spectrum.[38–40] While this can be advantageous for aesthetic façade features and improvements in PCE are indicative for economic viability (see Fig. 1), the lack of color neutrality limits its extensive utilization as building-integrated transparent PV solution.[2,41] Furthermore, the functional dependence on a transparent conductive oxide in comparison to a metal as back electrode introduces an additional trade-off between conductivity and transmittance, resulting also in larger PCE losses when upscaling from solar cells to modules.[17,42]

Non-wavelength-selective translucent PV is based on spatial segmentation of a conventional opaque solar cell stack across a transparent substrate. By introducing gaps in between photovoltaic active areas or entire solar cells, this approach provides almost color-neutral transmission of light while facilitating simple transparency variations. As the introduction of transparent areas increases the AVT and consequently reduces active photovoltaic area, the same trade-off between AVT and PCE as for semitransparent PV is evident. Initial research focused on the simple and versatile approach of macroscopically spacing silicon solar cells on glass substrates, becoming the dominant BIPV technology on the open market with PCEs reaching 18.9% at 10% AVT and 13.2% at 35% AVT for m^2 dimensions (see Fig. 1).[43,44] More recently, microstructural patterning of c-Si and thin-film PVs like a-Si or CIGS have become of interest as this promises to provide an improved, more homogeneous optical impression, particularly at viewing distances of a few meters or less. Available industry solutions based on a-Si provide up to 5.7% PCE at 10% AVT and 2.8% PCE at 30% AVT.[35,45] Regarding improvements in research at mm^2 to dm^2 device dimensions, Park *et al.* have recently demonstrated 25 cm^2 translucent c-Si solar cells with up to 14.5% PCE at 20% AVT *via* fabrication of micro holes utilizing deep reactive ion etching.[46] Focusing on thin-film PV, Tsai *et al.* employed laser-induced ablation to create transparent slits in commercial a-Si/μ-Si solar modules, achieving $\sim$6% PCE at $\sim$20% AVT.[47] Furthermore, Kuk *et al.* utilized laser scribing to create discrete microscopic circular transparent areas in CIGS cells of 0.46 cm^2 area, demonstrating 12% PCE at $\sim$12% AVT (estimated based on 15% transparent area ratio).[48] Depending on solution-based processing, Eperon *et al.* exploited spontaneous dewetting of

spin-coated perovskite films to create microscopic arrays of pores. While the AVT of resulting devices ranged from 7% to 30%, the PCEs corresponded to 7.6% and 3.5%, respectively.[49] Furthermore, investigating the effect of mechanically scribed and laser scribed transparent areas on the performance of fabricated translucent perovskite solar modules, Rakocevic *et al.* demonstrated devices with up to 13.1% PCE at 8% AVT and 5.4% PCE at 37% AVT and observed an over proportional decline in PCE beginning at AVTs above 30% and devices with more densely packed transparent areas.[50] While these results demonstrate the potential, the PCE of micro-patterned translucent PV devices has to be further improved and device areas upscaled before this technology becomes of interest for industry and is applied as BIPV for façades.[1,17] Additionally, the observed over proportional decline of PCE for increasing AVT values for translucent perovskite PV indicates the requirement for further process improvements to also provide efficient transparent PV solutions at 30–50% AVT.[49,50] Furthermore, few data has been so far presented regarding optical properties like CRI and haze, fundamentally defining this technology's optical appeal. In particular, neutral color rendering is expected to be crucial for wide public acceptance and overcoming architects' critical view of transparent PV as modern cityscapes are dominated by neutral colors of black, white and grey.[2,51] While translucent perovskite multi-junction devices have been envisaged and recognized as a promising path towards high efficiency neutral-color transparent PV, the tolerance of complex perovskite tandem stacks against extensive laser scribing has yet to be explored.

In response to these challenges, this work demonstrates micro-patterned translucent perovskite solar cells and submodules, enabling versatile shapes of transparent areas as well as transparency variations. Subsequent to the fabrication of devices, an in-depth analysis of electrical and optical performance allows for determination of optimal scribing parameters and shapes of transparent areas to mitigate over proportional losses even at AVTs above 30%. As future integration of transparent PVs in façades requires public acceptance, an investigation of optical properties of transmission and its perceptual quality is presented. Varying shapes of transparent areas and their spatial distribution, ideal designs are validated *via* analyses of view through images regarding neutral color rendering and level of haze utilizing ultraviolet/visible (UV/Vis) spectrophotometry. Finally, the optimized micro-patterning process is upscaled to monolithically interconnected submodules and transferred for the first time to 2-terminal perovskite–perovskite tandem cells, demonstrating the feasibility as well as future potential of high-efficiency translucent tandem PV. Additionally, the concept of arbitrary transmittance gradients *via* gradual change of density of introduced transparent areas is presented for the first time, providing new possibilities for architectural individualization. The laser patterning processes of translucent areas presented in this study are compatible with (and not limited to) perovskite absorber layer thicknesses of a wide range (400 nm to 1200 nm), which correspond also to the thickness of perovskite thin films realized with scalable fabrication methods like blade coating,[52] inkjet-printing,[53] slot-die coating[54] and evaporation.[55]

2. Results and discussion

Transparent and efficient translucent perovskite solar cells

Translucent perovskite-based PV requires a significant improvement in attainable PCEs, particularly avoiding the previously reported over proportional decline in efficiency at AVT values above 30%.[50] Furthermore, the development and optimization of a suitable manufacturing strategy must be based on simple, industrially applicable and reproducible processes. To address this challenge, a fast and accurate in-house laser scribing setup is employed to micro-pattern efficient opaque perovskite solar cells, demonstrating multiple shapes of transparent areas at optimized parameters.

In this context, perovskite-based PV combine excellent optoelectronic properties with the potential of solution-based fabrication. In addition, this approach facilitates the subsequent process transfer to perovskite–perovskite tandem solar cells to further increase the attainable maximum PCE. Here, perovskite solar cells using a planar solution-processed n–i–p architecture are processed in the sequence: indium tin oxide (ITO), (2-(9*H*-carbazol-9-yl)ethyl)phosphonic acid (2PACz), methylammonium lead iodide ($CH_3NH_3PbI_3$), fullerene (C_{60})/bathocuproine (BCP) and gold (Au) with an active area of 0.105 cm^2.[56] The employed custom-built laser scribing setup comprises an enclosed optical system attached to and a sample compartment inside a glovebox, thereby mitigating health risks posed by the laser and the sample's chemical constituents while allowing for good accessibility for maintenance. The optical system integrates a conventional nanosecond laser with frequency doubling (1064 nm, 532 nm) and a galvanometer scanner system enabling fast, precise and flexible laser scribing. Functional layers of the sample are protected from detrimental effects of oxygen, water and dust particles by the nitrogen atmosphere inside the glovebox. To mitigate adsorption of gases and debris resulting from laser scribing, the samples are under constant laminar nitrogen flow during the process. Exploiting the versatility of laser scribing, translucent solar cells based on transparent areas of different shapes are fabricated and their respective transmittance as well as their influence on solar cell performance are investigated. Scribing layouts for fabrication of individual transparent area shapes are depicted in Fig. S2 in the ESI.† Laser scribing parameters are individually optimized and different levels of AVT enabled by adapting the density (number per area) of transparent areas.

In the following, the fabricated translucent solar cells are characterized and the transmittance of transparent areas, the effect of the scribing process on characteristic resistances and the AVT-related PCE analyzed. Light microscopy images of the translucent perovskite solar cells are shown in Fig. 2a, inactive transparent areas now evenly distributed in the opaque cell stack. Regarding the choice of shapes for the transparent areas, the small circular transparent areas of 25 μm diameter

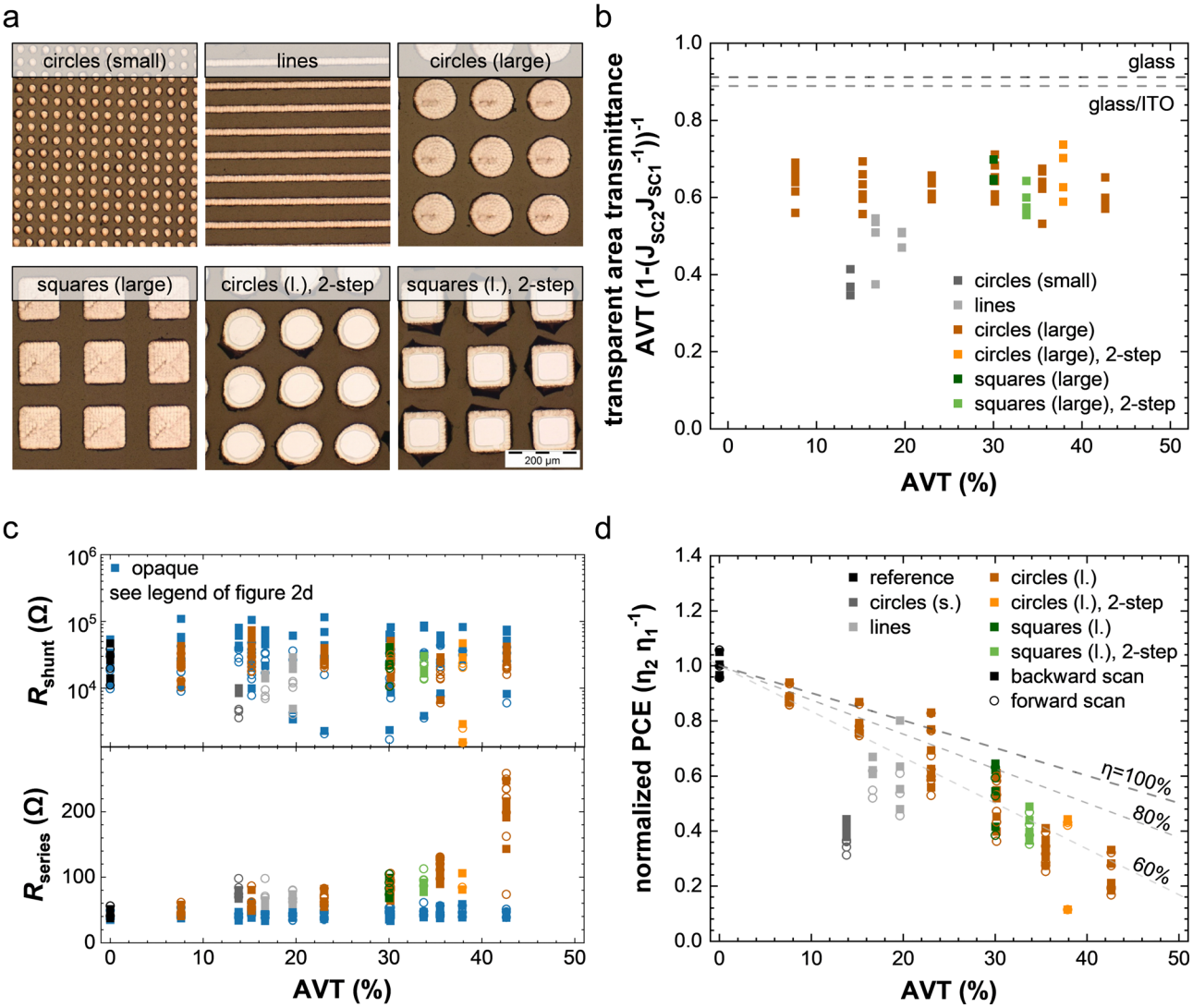

Fig. 2 Characterization of optical and electrical properties and performance of laser-based micro-patterned translucent perovskite solar cells, employing different transparent area shapes. (a) Light microscopy images of opaque perovskite solar cells and laser scribed transparent areas of different shapes. The scale bar in the lower right image applies to all images. (b) Transparent area transmittance of PSCs employing different transparent area shapes for a range of resulting AVT levels. (c) Shunt and series resistance of fabricated devices before (opaque) and after laser scribing of transparent areas. (d) Normalized PCEs of respective devices. Dashed lines are depicting the theoretical efficacy levels of devices as a function of retained PCE at respective AVT.

resemble the design introduced by Kuk *et al.* for translucent CIGS cells and are resulting from a single laser pulse.[48] The transparent areas in shape of lines, perpendicularly oriented to module interconnection lines and fabricated by overlapping pulse craters, were previously investigated by Rakocevic *et al.* and are of similar diameter.[50] As residual opaque materials significantly decrease the transmittance of scribed transparent areas and are particularly present at the ablation crater edges, due to the Gaussian laser intensity profile, two larger transparent area designs in circular and square shape are fabricated. Considering the angular resolution limit of a human eye of ~1 arcminute and targeting a homogeneous optical impression for all BIPV applications with >50 cm viewing distance, the diameter of large transparent areas was set to 120 µm.[57] When scribing circles/squares from the outer edge towards the center, the ratio of highly transparent area is increased, as shown in Fig. 2a. Additionally, to exploit the superior AVT of glass (~91%) in comparison to glass/ITO (~88%) as shown in Fig. S3 in the ESI,† a second laser scribing step (2-step) at elevated laser fluence is performed to remove the ITO. Restricting the removal to the inner part of the transparent area mitigates a detrimental effect of the stronger lasing pulses on the surrounding layer stack, while also inhibiting this approach's implementation for the first two introduced transparent area designs (small circles, lines). While the resulting transparent areas demonstrate the central removal of ITO as well as further improvement in ablation of residuals, the higher intensity led to occasional formation of back contact flakes.

Next, translucent perovskite solar cells are optically and electrically characterized (see Fig. S4 in the ESI† for a detailed comparison of absolute photovoltaic parameters). Depicting the transmittance efficiency of scribed transparent areas, Fig. 2b utilizes the ratio of short-circuit-current–density (J_{SC}) after and before scribing, respectively, to normalize the measured AVT values (transparent area transmittance). This corresponds to a normalization with the photovoltaic active area. The transparent areas in shape of small circles as well as stripes show transmittance efficiencies of 0.4 to 0.5, proving the profoundly detrimental effect of residues. The four larger shapes, introduced to decrease the ratio of outer partial ablation to inner complete ablation of layers, demonstrate superior transmittance efficiencies of 0.6 to above 0.7. Transparent areas with additional central ITO ablation show only slight transmittance efficiency improvements, as positive effects of higher transmittance are assumed to cancel out with the additional reduction in J_{SC} due to the unintended back contact flake formation. Further optimization of scribing parameters is expected to avoid respective flakes.

Having a decisive impact on the fill factor (FF) of devices and, thereby, their performance, the influence of the scribing process and transparent area shapes on shunt and series resistance of cells is investigated. In particular, the decrease in shunt resistance is a common problem for laser-induced material removal due to detrimental shunt paths that originate from melting or flaking of the ablated back contact. As optimized process parameters lead to almost complete mitigation of these phenomena, Fig. 2c (top) shows the absence of detrimental effects on the shunt resistance. Variations of the latter manifest as statistical distribution around the reference value. As depicted in Fig. 2c (bottom) the normalized series resistance is steadily increasing for all shapes, reaching a factor of two at AVTs of 30 to 35%, whereas a further increase in AVT leads to a significantly accelerated rise. This is in good agreement with expectations as back and front contact are spatially ablated, reducing the cross section and thereby conductivity of respective layers, ultimately tending to 0. Considering the simultaneous reduction in current density, a linear increase of the series resistance of similar amplitude result in constant ohmic losses (see Fig. S5, ESI†). However, at AVTs greater than 35%, an over proportional increase in series resistance is evident, expected ohmic losses rising by a factor of up to ~ 4, rendering this a limiting factor. An increase in back contact layer thickness or a decrease in cell width of future modules can decrease this detrimental effect.

Comparing the overall process quality, the PCE relative to the AVT of devices is normalized with the initial PCE before scribing and presented in Fig. 2d (see Fig. S4a in the ESI† for absolute values). It should be noted that the device's resulting AVT divided by its relative loss in PCE is found to be a good indicator for process efficiency. Taking the maximum AVT of glass of 91% and of a glass/ITO layer stack of 88% into consideration, the effective optimum for the developed scribing process lies in between. To provide a visualization aid, process efficiency levels for given reference solar cells are depicted *via* three dashed lines. As a consequence, from the inferior transparent area transmittances, devices with transparent areas in shape of small circles and stripes show strong over-proportional decrease in PCE for AVTs of 16–21%. In contrast, the devices with large circular transparent areas demonstrate almost optimal results up to 24% AVT. Further increase in AVT results for all four large transparent area shapes in a stronger decline, reaching a process efficiency of 70% for an AVT of 44% (see Fig. 2d) due to the observed significant increase in series resistance (see Fig. 2c). Champion devices demonstrate PCEs of 16.2%, 13.9% and 8.1% at AVTs of 8%, 15% and 38%, respectively, as depicted in Fig. 1. The constant PCE decline to down to 30% in AVT emphasizes the benefits of larger multi-pulse-based transparent areas as well as the achieved good process quality. However, further reduction of back contact and the corresponding increase in series resistance become a limiting factor for translucent devices above 30% AVT independent of chosen transparent area shapes. The assessment of short-term device stability, as depicted in Fig. S6 of the ESI,† indicates no scribing induced instabilities or accelerated degradation.

Appearance of translucent perovskite photovoltaics for BIPV

Having developed laser scribing layouts and corresponding scribing process parameters that provide highly transparent areas as well as a reduced decline in PCE for higher AVTs, the optical impression and appearance are investigated next. Here, we demonstrate that the new transparent area shapes with optimized scribing process exhibit a significant improvement in color rendering and image clarity.

In order to allow for the qualitative and quantitative assessment of optical properties from a perceptual point of view, the translucent device areas are scaled up by a factor of 40 to solar cell layer stacks of 4 cm^2 aperture area. All translucent devices are fabricated with a targeted AVT of 30%. While slight variations of this value may influence the qualitative optical impression, all quantitative evaluations are designed as to be independent of the absolute transmittance and are only affected by the ablation behavior of individual transparent areas.

For a qualitative analysis, pictures of the front and back side of the resulting devices, as well as view-through images, are depicted in Fig. 3a. For all designs, homogenous and defect-free translucent areas over the complete aperture area are evident, demonstrating the consistent quality of the developed scribing processes. An in-detail view of fabricated transparent areas as well as an exemplary presentation of the optimization process is provided in Fig. S7–S9 in the ESI† *via* microscopy and vertical scanning interferometry images and confirms the flake- and residual-free ablated transparent areas. Regarding the overall optical impression, patterns are observed for pictures of front and back side on most samples (see Fig. 3a). These patterns are not visible by naked eye but result from the moiré effect. They appear due to the superposition of two periodic patterns, in this case the fabricated transparent areas and the pixel-based displays for examining taken pictures.[58] The moiré effect can be avoided by spatial randomization of the fabricated transparent areas, as depicted in Fig. S10 in the ESI.† As the

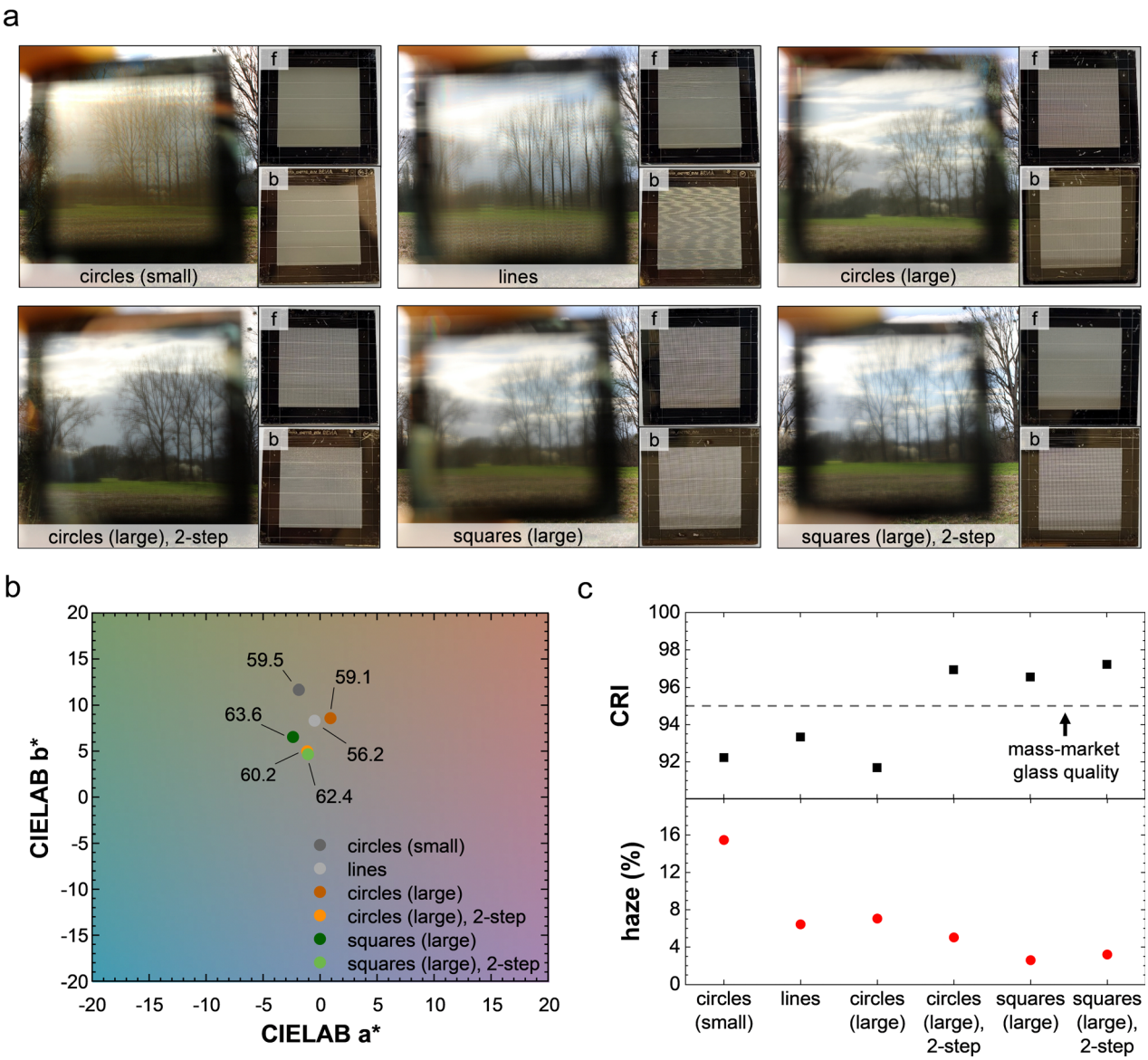

Fig. 3 Characterization of optical properties of translucent perovskite based solar submodules with 4 cm^2 aperture area, comprising 5 monolithically interconnected cells. (a) View-through, front side and back side images of translucent submodules with the previously introduced transparent area formats. (b) CIELAB chromaticity coordinates a^* and b^* of measured transmittance spectra of fabricated translucent areas. Perceptual lightness L^* of sample areas are depicted *via* inserted numbers. (c) Color rendering index (top) and haze (bottom) of translucent areas.

dimensions of fabricated transparent areas (>25 μm) and respective periodicity (>40 μm) greatly exceed the wavelengths of visible light, no diffraction colors can be observed. Considering the most important evaluation criteria of view-through images, the big square design as well as both shapes with additional ITO ablation demonstrate superior clarity and crispness of objects.

Allowing for a quantification of the observed variations of aesthetic quality, first, UV/Vis/NIR spectrophotometry measurements are performed for all samples (see Fig. S11 in the ESI†) and the CIELAB chromaticity coordinates for the transmission spectra are calculated. The calculations are described in the ref. 59–61. All results are summarized in Table S2 in the ESI.† The resulting chromaticity coordinates are depicted in Fig. 3b and show significant differences in positive b* values, being synonymous in magnitude of yellowish tinting and ranging from 11.7 down to 4.7. The square design shows already good color rendering with $a^* = -2.4$ and $b^* = 6.5$. The additional ITO ablation further enhances this to excellent, almost neutral color rendering of $a^* = -1.1$ and $b^* = 4.7$, their chromaticity coordinates being in the established color fidelity of the international architectural glass market ($5 < a^* < 1$ and $5 < b^* < 5$).[59,62] The respective CRI values, which pose a key figure-of-merit in the glass industry and are interdependent with the chromaticity coordinates, are depicted in Fig. 3c. The CRI of up to 97.2 for the square shapes with ablated ITO confirms the suitability for architectural applications, as CRIs > 95 being in the accepted range of yellowish tinted glass. Last, the previous observed

differences in view-through image crispness or levels of distortions are quantitatively evaluated utilizing the ratio of diffuse ($>3.8^\circ$ deviation from angle of incidence) to total transmittance of translucent areas (haze). Having the highest ratio of crater edge area to transparent area, the small circles show a high level of scattering with ~16% haze. In contrast, significant improvements are demonstrated by the other shapes, squares demonstrating again superior optical properties of down to 3% haze.

In consequence of regulatory requirements, strategies to reduce lead leakage of perovskite-based PV devices become highly relevant for systems in close proximity to humans like BIPV in particular, but can affect device performance and appearance.[63] Developed solutions can be categorized in physical barriers that prevent invasion or leakage of water and oxygen, and chemisorption layers that chemically absorb and bind free-state lead. For both categories, solutions as external coating (*e.g.* self-healing epoxy resin,[64] cation exchange resin[65]) and internal within the functional solar cell stack (*e.g.* lead sulfate shell,[66] lead chelation[67]) are available. As these strategies were developed to also be applicable for the transparent front side of perovskite photovoltaics, optimized approaches demonstrate minimal transmittance losses.[68] Accordingly, their application is expected to only negligibly affect the transmittance and color impression of translucent devices while in particular internal encapsulation or chemisorption layers are compatible with the developed laser scribing process.

Technological outlook – proof of concepts

The optimization of lasing parameters and adaption of transparent area shapes led so far to a significant improvement of retained PCEs of solar cells, as well as neutral color rendering and minimal haze that make this concept suitable for BIPV. However, additional requirements for a successful transfer to industrial manufacturing are scalability and further enhancement of achievable PCEs. Consequently, we investigate in the following whether a similar quality of devices can be obtained when fabricating submodules, and whether the developed process can be applied to more efficient and complex tandem perovskite solar cells. As BIPV also comprises the aspect of aesthetics in regard to public acceptance, a concept for varying transmittance within one substrate is explored lastly, potentially providing an opportunity for architectural individualizations and unique façades.

Translucent perovskite submodules. The translucent device areas are scaled up by a factor of 40 from solar cells of 0.105 cm^2 to submodules of 4 cm^2 aperture area, comprising 5 cells (à 20 mm × 4 mm). The monolithic series interconnections are fabricated *via* laser scribing of the established P1–P2–P3 lines.[69] Subsequently, the translucent areas are fabricated by employing optimized lasing parameters and targeting an AVT of 30%.

The champion submodule demonstrates a PCE of 9.0% at 32% AVT, with a fill factor (FF) of 74%, an open-circuit voltage (V_{OC}) of 5.5 V, and a short-circuit current density ($J_{SC,\ subcell}$) of 11.1 mA cm^{-2} in backward scan direction. Considering the forward scan direction with a PCE of 8.3%, a FF of 70%, a V_{OC} of 5.4 V, and a $J_{SC,\ subcell}$ of 11.0 mA cm^{-2}, only minimal *J–V* hysteresis is evident (see Fig. 4a). Furthermore, the submodule active area exhibits highly neutral color rendering with a CRI of 95.1 and a perceptually homogenous impression, as shown in

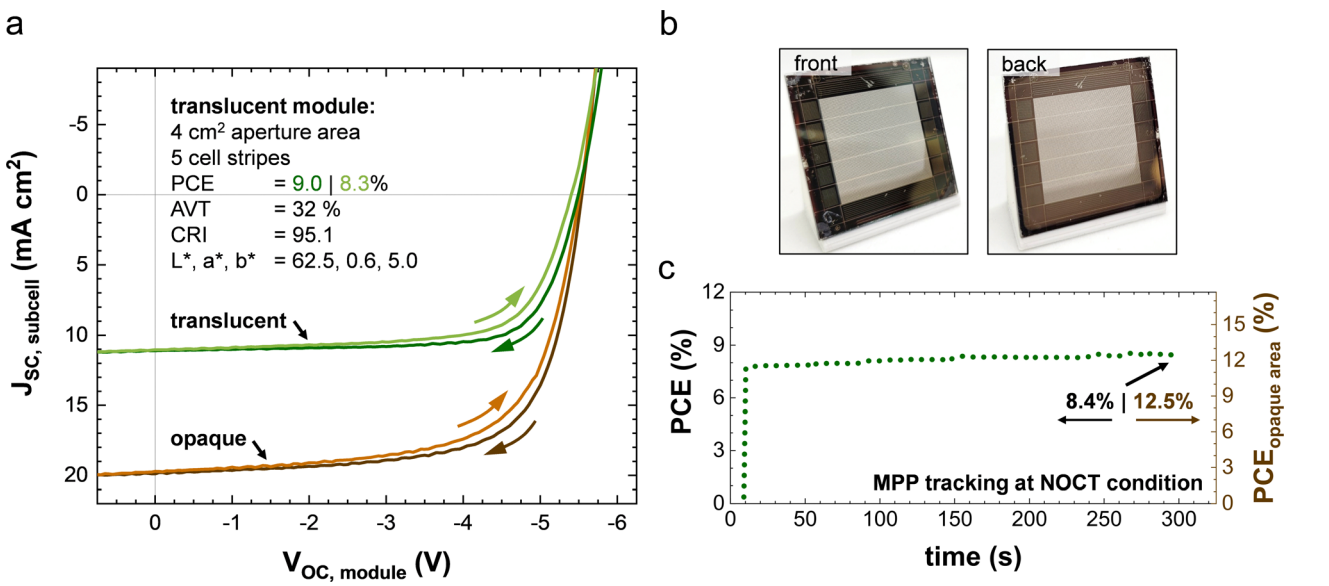

Fig. 4 Electrical and optical characterization of the best-performing translucent perovskite submodule with 4 cm^2 aperture area and 5 monolithically interconnected subcells. (a) *J–V* characteristics of the champion submodule before (opaque) and after (translucent) fabrication of transparent areas *via* laser scribing. The inset states basic optical properties of the translucent area. (b) Front side and back side images of the translucent perovskite submodule. (c) Short-term stability under continuous illumination during maximum power point (MPP) tracking at nominal operating cell temperature conditions (NOCT) without active cooling. For comparison, the absolute PCE and opaque area PCE (PCE·[1-AVT]-1) are depicted on the left and right axis, respectively.

Fig. 4b. A photon balance consistency check is depicted in Fig. S12 in the ESI.† The slight increase in stabilized PCE for maximum power point (MPP) tracking under nominal operating cell temperature (NOCT) conditions, as depicted in Fig. 4c, is attributed to light soaking. Compared to the PCE of this submodule before introducing transparent areas of 15.2% (14.4%), the submodule retains 59.2% (57.6%) of PCE after introduction of transparent areas (see Table S3 in the ESI†). The process efficiency of this module of 79% (76%) is emphasized, highlighting the high quality of the developed scribing process and the feasibility of upscaling this process to fabricate efficient translucent modules.

Perovskite–perovskite 2-terminal tandem photovoltaics. Besides demonstrating the feasibility of upscaling translucent perovskite photovoltaics, envisaging a path towards higher efficiencies is similarly important. In this regard, devices with higher PCEs typically comprise more layers with sophisticated purposes, increasing the devices complexity and thereby risks of light or heat induced degradation when suspended to the developed scribing process. In particular 2-terminal perovskite–perovskite (2TPP) tandem photovoltaics are of interest, potentially reaching higher PCEs by harvesting light in a broader range of wavelengths more efficiently and implicitly comprising more functional layers.[22,23] Therefore, the developed process is transferred to 2TPP tandem solar cells and the device and process performance evaluated.

The utilized 2TPP tandem solar cells are based on the layer stack sequence of IOH, 2PACz, wide bandgap perovskite with a 1.78 eV bandgap ($FA_{0.8}Cs_{0.2}(I_{0.6}Br_{0.4})_3$), LiF, C_{60}, SnO_x, ITO, PEDOT:PSS, narrow bandgap perovskite with a 1.26 eV bandgap ($Cs_x(FA_{0.83}MA_{0.17})_{(1-x)}Sn_{0.5}Pb_{0.5}I_3$), PCBM, C_{60}, BCP and Au as depicted in Fig. 5a.[70] The active area was defined by utilizing a shadow mask of 8.1 mm^2 area. After reference measurements were performed, transparent areas were fabricated by utilizing established scribing designs with adapted lasing parameters, targeting AVTs of 10% and 30%.

The champion tandem solar cells demonstrate PCEs as high as 17.7% at 12% AVT and 11.1% at 31% AVT, respectively, with FFs of 77% and 71%, V_{OC} of 1.95 V and 1.94 V, and J_{SC} of 11.9 mA cm^{-2} and 8.1 mA cm^{-2} in backward scan direction. Considering the forward scan direction with PCEs of 15.0% and 9.3%, FFs of 68% and 61%, V_{OC} of 1.94 V and 1.94 V, and J_{SC} of 11.4 mA cm^{-2} and 7.9 mA cm^{-2}, slight *J–V* hysteresis is evident, as shown in Fig. 5b and c. However, this stems from the device stack itself, as hysteresis is already present during reference measurements before introducing the transparent areas (see also Table S4 in the ESI†). Regarding optical properties, both tandem solar cells demonstrate excellent color rendering with a CRIs of 95.1 and 95.5, respectively, while the translucent areas are perceptually uniform. The photon balance consistency checks are documented in Fig. S13 and S14 in the ESI.† Evaluating the process efficiency by comparing device performance before and after introducing transparent areas, the tandem solar cells retain 86% (87%) and 60% (61%) PCE in backward (forward) scan direction. This results in process efficiencies of ≈79% and ≈77%, successfully demonstrating the transfer to more complex layer stacks at consistently high optical and electrical device quality. Following subsequent upscaling, a translucent tandem mini-module with 12.25 cm^2 aperture area, similar device architecture and fabricated *via* fully scalable deposition methods provides promising 10.3% PCE at 15% AVT while further optimizations are envisaged to close the gap towards tandem solar cells (see Table S5 and Fig. S15, S16 in the ESI†).

With regard to the readiness of transferring the presented process to industrial production, we note that our demonstration of high-quality translucent areas on spin-coated PSCs, scalable blade-coated perovskite solar modules as well as for complex 2T tandem PSCs proves the robustness of the developed laser scribing process, which can be effectively applied to a variety of perovskites, including those deposited with scalable methods. However, besides adaptation to other device architectures, the laser patterning process is required to demonstrate throughputs that are compatible with inline manufacturing, typically requiring production cycle times for

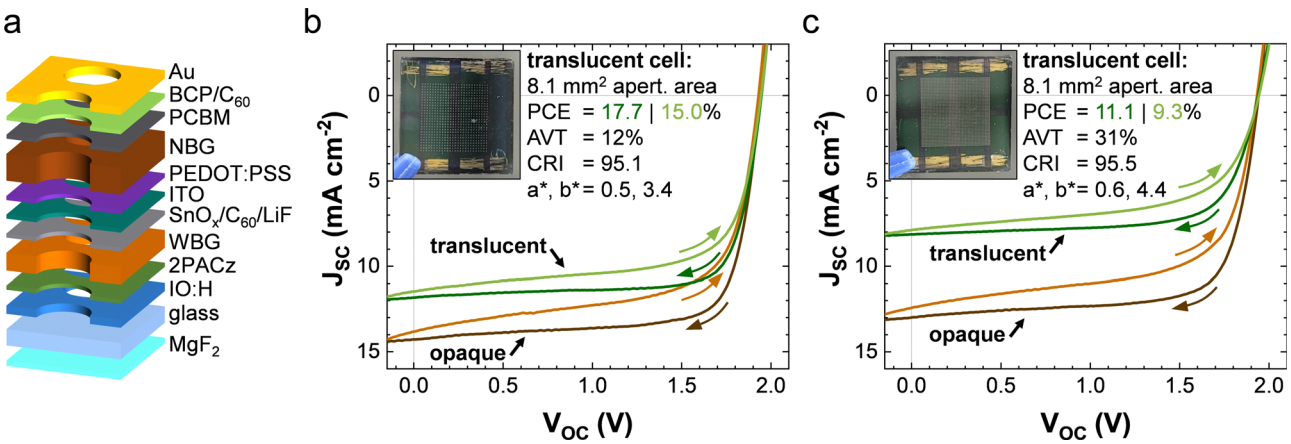

Fig. 5 (a) Employed layer stack sequence for the fabrication of the first translucent 2-terminal perovskite–perovskite tandem solar cells. (b and c) *J–V* characteristics of best-performing tandem solar cells with 8.1 mm^2 aperture area before (opaque) and after (translucent) fabrication of transparent areas at 12% AVT (b) and 31% AVT (c). The insets depict the respective front side and basic optical properties of the translucent areas.

one m^2 solar module in the range of minutes. Given the widespread nature of laser patterning in today's industrial thin film solar module fabrication, several strategies like (1) a high rate pulsed laser source (10 MHz) instead of the 10 kHz patterning frequency used in our laboratory scale tool, or (2) applying multiple galvanometer scanners in parallel[71] are readily available to significantly increase the throughput of the laser patterning process (3–4 orders of magnitude). Utilizing these strategies to improve the instrumentation combined with process optimization (*e.g.* pulse overlap, line overlap), the process throughput of the presented laser patterning of translucent perovskite solar modules can be lowered to the range of minutes. Eqn (S1) in the ESI† shows that the fabrication time for translucent areas with ~30% AVT can be reduced from current times of ~25 s cm^{-2} (~4000 min m^{-2}) to ~2 min m^{-2}.

Design opportunities *via* transmittance gradients. In addition to meeting performance and AVT targets, BIPV always includes aspects of perception and aesthetics, as these are key to public acceptance. In this regard, the process' flexibility offers next to fabrication of variable transparent areas on different thin-film stacks the possibility of changing the spatial distribution of the transparent areas. By continuously changing the distribution density over the substrate area, transmittance gradients are generated and their optical impression in the following demonstrated.

For demonstration, submodules, as previously introduced, with 4 cm^2 aperture area were used and transparent area scribing designs *via* in-house MATLAB (MathWorks, USA) script generated. As proof of concept of arbitrary and complex gradient designs, we present three different designs that demonstrate feasibility and effective current matching. Hereby, the first design, featuring a gradient that runs parallel to connection lines and thus horizontally, represents the fundamental variant. The gradient of the second design runs perpendicular to interconnection lines (vertical) and requires a transmittance-dependent adaption of cell widths in order to prevent current mismatch and resulting PCE losses. The third design introduces a radial gradient, the origin being centered in the module's aperture area, and likewise requires cell width adaptions. All cell width adaptions are realized by estimation of the integrated cell currents after the laser scribing. The resulting transmittances were measured for two individual areas with the largest expected difference.

The champion submodules with employed transmittance gradients are depicted in Fig. 6 and demonstrate a homogeneous and defect-free scribing result, distinctly featuring the optical effect of the transmittance gradients. Furthermore, shown submodules achieved AVT gradients from 31% to 7% for the horizontal, from 33% to 5% for the vertical, and from 28% to 8% for the radial design, equating to an absolute change of transmittance of up to ≈7% cm^{-1}. Further regarding optical properties, it should be noted that some CRIs stray below the desired threshold of 95, making further optimization of lasing parameters desirable. Besides, the submodules show good electrical performance with PCEs of 12.0% (11.3%) for horizontal, 10.3% (9.8%) for vertical and 11.2% (10.2%) for radial gradients in backward (forward) scan direction, while MPP measurements at NOCT condition over 300 s verify the stable behavior (see Fig. S17 and S18 in the ESI†). Furthermore, the adaption of cell widths enabled significant current matching improvements, reducing the maximum current mismatch of subcells for vertical gradients from $35\%_{rel}$ to only $15\%_{rel}$ and for radial gradients from 22%rel to $6\%_{rel}$ (see Fig. S19 in the ESI†). The devices successfully demonstrate the good electrical performance as well as uniform optical impression of the implemented transmittance gradients, being enabled by the versatile laser scribed translucent photovoltaics.

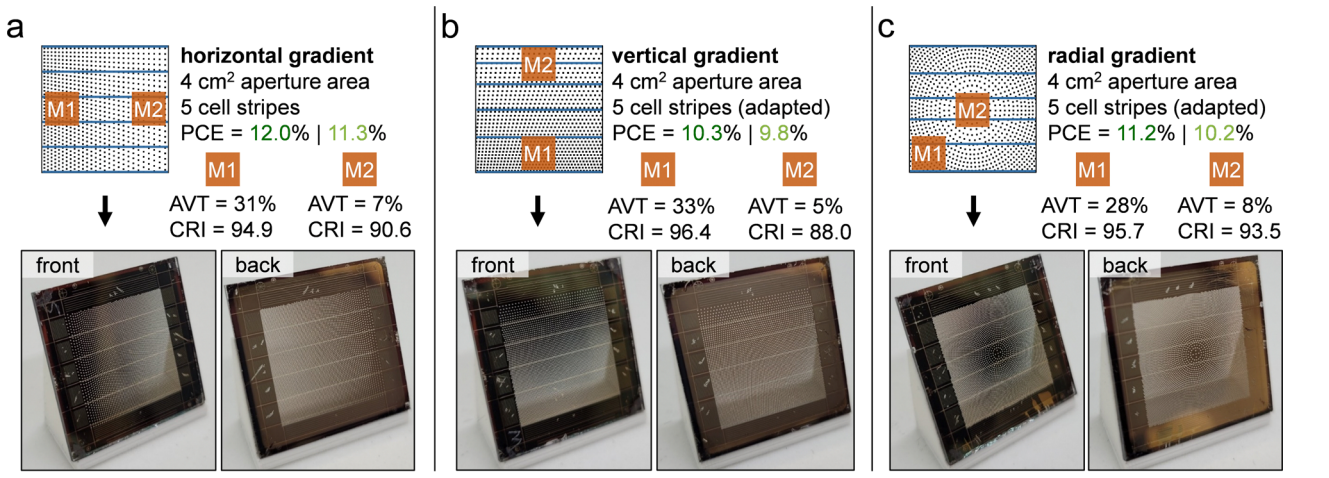

Fig. 6 Concept, implementation and characterization of transmittance gradients in translucent perovskite submodules with 4 cm^2 aperture area and 5 monolithically interconnected subcells. Laser scribing layouts (respectively top left) for transparent areas with different spatial distributions and adapted interconnection lines based on the concept of (a) horizontal, (b) vertical and (c) radial transmittance gradients. Basic electrical and optical properties (respectively top right) of translucent areas of champion submodules with transmittance gradients. Back side and front side (respectively bottom left and right) image of fabricated submodules.

3. Conclusions

This work reports on translucent perovskite photovoltaics, highlighting the scalable fabrication of efficient translucent PV devices for single-junction as well as tandem architectures, while obtaining optical qualities suited for BIPV. Utilizing a custom-built laser scribing setup, the fabrication of different transparent area shapes with diameters down to 25 μm is optimized and minimal detrimental effect on the electrical performance of perovskite solar cells for AVTs of up to 44% realized. The resulting translucent areas exhibit a uniform appearance, demonstrating industrial glass quality through neutral color rendering with CRIs as high as 97 and minimal haze of down to 3%. The process transfer to submodules with 4 cm^2 aperture area yields PCEs of up to 9.0% (8.4% sPCE) at 32% AVT and a process efficiency of 79% (ratio of AVT gain over relative PCE loss) at similar optical quality, highlighting the ease of upscaling this fabrication technique. Furthermore, the subsequent transfer to two-terminal perovskite–perovskite tandem solar cells with PCEs as high as 17.7% at 12% AVT and 11.1% at 31% AVT and process efficiencies of up to 79% demonstrates to the best of our knowledge the first translucent perovskite tandem solar cells. Lastly, the concept of transmittance gradients within modules and cells is presented, submodules featuring an absolute change of transmittance as high as 7% cm^{-1} and up to 12.0% PCE, successfully providing a foundation for new applications and architectural individualizations.

Author contributions

Conceptualization, D. B. R., T. A. and U. W. P.; methodology, D. B. R.; software: D. B. R.; investigation, D. B. R., B. A. N., M. A. P.-R., S. G., H. H., A. D., T. F.; resources, B. S. R. and U. W. P.; writing – original draft, D. B. R.; funding acquisition, B. S. R. and U. W. P.; supervision, T. A., B. S. R. and U. W. P.

Conflicts of interest

There are no conflicts to declare.

Acknowledgements

The authors are grateful for the great spirit of the Taskforce Perovskite Photovoltaics at KIT and the scientific discussions. Financial support by the Initiating and Networking funding of the Helmholtz Association (HYIG of U.W.P. (VHNG- 1148)), the Helmholtz Energy Materials Foundry (HEMF), the Solar Technology Acceleration Platform (Solar TAP) funded by the Helmholtz Association, the program oriented funding IV of the Helmholtz Association (Materials and Technologies for the Energy Transition, Topic 1: Photovoltaics and Wind Energy, Code: 38.01.04), the German Federal Ministry for Economic Affairs and Climate Action (BMWK) through the project CAPITANO (03EE1038B), and the Karlsruhe School of Optics & Photonics (KSOP) is gratefully acknowledged. The project is further supported by European Union's Horizon 2020 research and innovation program under grant agreement No 850937, project PERCISTAND.

Notes and references

1 H. Gholami, H. N. Røstvik and D. Müller-Eie, Holistic economic analysis of building integrated photovoltaics (BIPV) system: Case studies evaluation, *Energy Build.*, 2019, **203**, 109461, DOI: **10.1016/j.enbuild.2019.109461**.
2 P. Heinstein, C. Ballif and L. E. Perret-Aebi, Building integrated photovoltaics (BIPV): Review, potentials, barriers and myths, *Green*, 2013, **3**, 125–156, DOI: **10.1515/green-2013-0020**.
3 US Energy Information Administration EIA (2016). Commercial Buildings Energy Consumption Survey (CBECS) Data (US Energy Information Administration, 2012). Commer. Build. Energy Consum. Surv., Table B1.
4 Z. Li, T. Ma, H. Yang, L. Lu and R. Wang, Transparent and Colored Solar Photovoltaics for Building Integration, *Sol. RRL*, 2021, **5**, 1–21, DOI: **10.1002/solr.202000614**.
5 N. Jakica, State-of-the-art review of solar design tools and methods for assessing daylighting and solar potential for building-integrated photovoltaics, *Renewable Sustainable Energy Rev.*, 2018, **81**, 1296–1328, DOI: **10.1016/j.rser.2017.05.080**.
6 Y. He and M. A. Schnabel, An approach for daylight calculation of a building integrated photovoltaic (BIPV) Façade, *Archit. Sci. Rev.*, 2018, **61**, 226–233, DOI: **10.1080/00038628.2018.1470964**.
7 K. Lee, H. D. Um, D. Choi, J. Park, N. Kim, H. Kim and K. Seo, The Development of Transparent Photovoltaics, *Cell Rep. Phys. Sci.*, 2020, **1**, 100143, DOI: **10.1016/j.xcrp.2020.100143**.
8 D. Liu, C. Yang and R. R. Lunt, Halide Perovskites for Selective Ultraviolet-Harvesting Transparent Photovoltaics, *Joule*, 2018, **2**, 1827–1837, DOI: **10.1016/j.joule.2018.06.004**.
9 G. Liu, C. Wu, Z. Zhang, Z. Chen, L. Xiao and B. Qu, Ultraviolet-Protective Transparent Photovoltaics Based on Lead-Free Double Perovskites, *Sol. RRL*, 2020, **4**, DOI: **10.1002/solr.202000056**.
10 Y. Li, C. Ji, Y. Qu, X. Huang, S. Hou, C. Z. Li, L. S. Liao, L. J. Guo and S. R. Forrest, Enhanced Light Utilization in Semitransparent Organic Photovoltaics Using an Optical Outcoupling Architecture, *Adv. Mater.*, 2019, **31**, 1–8, DOI: **10.1002/adma.201903173**.
11 X. Zhang, Y. Qian, X. Ling, Y. Wang, Y. Zhang, J. Shi, Y. Shi, J. Yuan and W. Ma, α-CsPbBr3Perovskite Quantum Dots for Application in Semitransparent Photovoltaics, *ACS Appl. Mater. Interfaces*, 2020, **12**, 27307–27315, DOI: **10.1021/acsami.0c07667**.
12 D. Liu, C. Yang, P. Chen, M. Bates, S. Han, P. Askeland and R. R. Lunt, Lead Halide Ultraviolet-Harvesting Transparent Photovoltaics with an Efficiency Exceeding 1%, *ACS Appl. Energy Mater.*, 2019, **2**, 3972–3978, DOI: **10.1021/acsaem.9b00270**.

13 C. Yang, W. Sheng, M. Moemeni, M. Bates, C. K. Herrera, B. Borhan and R. R. Lunt, Ultraviolet and Near-Infrared Dual-Band Selective- Harvesting Transparent Luminescent Solar Concentrators, *Adv. Energy Mater.*, 2021, **11**(12), DOI: **10.1002/aenm.202003581**.

14 Q. Huaulmé, V. M. Mwalukuku, D. Joly, J. Liotier, Y. Kervella, P. Maldivi, S. Narbey, F. Oswald, A. J. Riquelme and J. A. Anta, *et al.*, Photochromic dye-sensitized solar cells with light-driven adjustable optical transmission and power conversion efficiency, *Nat. Energy*, 2020, **5**, 468–477, DOI: **10.1038/s41560-020-0624-7**.

15 J. M. Andrés Castán, V. M. Mwalukuku, A. J. Riquelme, J. Liotier, Q. Huaulmé, J. A. Anta, P. Maldivi and R. Demadrille, Photochromic spiro-indoline naphthoxazines and naphthopyrans in dye-sensitized solar cells, *Mater. Chem. Front.*, 2022, **6**(20), 2994–3005, DOI: **10.1039/d2qm00375a**.

16 O. Almora, D. Baran, G. C. Bazan, C. Berger, C. I. Cabrera, K. R. Catchpole, S. Erten-Ela, F. Guo, J. Hauch and A. W. Y. Ho-Baillie, *et al.*, Device Performance of Emerging Photovoltaic Materials (Version 2), *Adv. Energy Mater.*, 2021, **11**(48), DOI: **10.1002/aenm.202102526**.

17 C. J. Traverse, R. Pandey, M. C. Barr and R. R. Lunt, Emergence of highly transparent photovoltaics for distributed applications, *Nat. Energy*, 2017, **2**, 849–860, DOI: **10.1038/s41560-017-0016-9**.

18 A. Shankar, K. Vijayakumar and B. C. Babu Techno-economic and energy assessment of building integrated photovoltaic module as an envelope of the building, DOI: **10.1002/2050-7038.13105**.

19 C. J. Traverse, P. Chen and R. R. Lunt, Lifetime of Organic Salt Photovoltaics, *Adv. Energy Mater.*, 2018, **8**, 1–7, DOI: **10.1002/aenm.201703678**.

20 C. J. Traverse, M. Young, J. Suddard-Bangsund, T. Patrick, M. Bates, P. Chen, B. Wingate, S. Y. Lunt, A. Anctil and R. R. Lunt, Anions for Near-Infrared Selective Organic Salt Photovoltaics, *Sci. Rep.*, 2017, **7**, 1–8, DOI: **10.1038/s41598-017-16539-3**.

21 E. Ravishankar, R. E. Booth, C. Saravitz, H. Sederoff, H. W. Ade and B. T. O'Connor, Achieving Net Zero Energy Greenhouses by Integrating Semitransparent Organic Solar Cells, *Joule*, 2020, **4**, 490–506, DOI: **10.1016/j.joule.2019.12.018**.

22 W. Shockley and H. Queisser, Detailed balance limit of efficiency of p-n junction solar cells, *Renewable Energy*, 2018, **2–4**, 35–54, DOI: **10.4324/9781315793245-44**.

23 R. R. Lunt, Theoretical limits for visibly transparent photovoltaics, *Appl. Phys. Lett.*, 2012, **101**, 1–4, DOI: **10.1063/1.4738896**.

24 O. Almora, D. Baran, G. C. Bazan, C. Berger, C. I. Cabrera, K. R. Catchpole, S. Erten-Ela, F. Guo, J. Hauch and A. W. Y. Ho-Baillie, *et al.*, Device Performance of Emerging Photovoltaic Materials (Version 1), *Adv. Energy Mater.*, 2021, **11**(11), DOI: **10.1002/aenm.202002774**.

25 R. R. Lunt and V. Bulovic, Transparent, near-infrared organic photovoltaic solar cells for window and energy-scavenging applications, *Appl. Phys. Lett.*, 2011, **98**(11), DOI: **10.1063/1.3567516**.

26 C. C. Chen, L. Dou, R. Zhu, C. H. Chung, T. B. Song, Y. B. Zheng, S. Hawks, G. Li, P. S. Weiss and Y. Yang, Visibly transparent polymer solar cells produced by solution processing, *ACS Nano*, 2012, **6**, 7185–7190, DOI: **10.1021/nn3029327**.

27 L. Zuo, X. Shi, W. Fu and A. K. Y. Jen, Highly Efficient Semitransparent Solar Cells with Selective Absorption and Tandem Architecture, *Adv. Mater.*, 2019, **31**, 1–9, DOI: **10.1002/adma.201901683**.

28 C. Yang, M. Moemeni, M. Bates, W. Sheng, B. Borhan and R. R. Lunt, High-Performance Near-Infrared Harvesting Transparent Luminescent Solar Concentrators, *Adv. Opt. Mater.*, 2020, **8**, 1–6, DOI: **10.1002/adom.201901536**.

29 C. Yang, H. A. Atwater, M. A. Baldo, D. Baran, C. J. Barile, M. C. Barr, M. Bates, M. G. Bawendi, M. R. Bergren and B. Borhan, *et al.*, Consensus statement: Standardized reporting of power-producing luminescent solar concentrator performance, *Joule*, 2022, **6**, 8–15, DOI: **10.1016/j.joule.2021.12.004**.

30 C. Yang and R. R. Lunt, Limits of Visibly Transparent Luminescent Solar Concentrators, *Adv. Opt. Mater.*, 2017, **5**, 1–10, DOI: **10.1002/adom.201600851**.

31 Glaswerke Arnold Merkendorf GmbH & Co. (2008). Solar Architecture. Voltarlux.

32 Schott Solar GmbH (2010). ASI THRU thin-film solar module, semitransparent.

33 J. Romaní, A. Ramos and J. Salom, Review of Transparent and Semi-Transparent Building-Integrated Photovoltaics for Fenestration Application Modeling in Building Simulations, *Energies*, 2022, **15**(9), DOI: **10.3390/en15093286**.

34 Polysolar Limited (2022). PS-CT series panels.

35 Onyx Solar Group LLC (2022). Amorphous Silicon PV Glass.

36 D. Yang, X. Zhang, Y. Hou, K. Wang, T. Ye, J. Yoon, C. Wu, M. Sanghadasa, S. F. Liu and S. Priya,). 28.3%-Efficiency Perovskite/Silicon Tandem Solar Cell By Optimal Transparent Electrode for High Efficient Semitransparent Top Cell, *Nano Energy*, 2021, **84**, 105934, DOI: **10.1016/j.nanoen.2021.105934**.

37 N. Chaturvedi, N. Gasparini, D. Corzo, J. Bertrandie, N. Wehbe, J. Troughton and D. Baran, All Slot-Die Coated Non-Fullerene Organic Solar Cells with PCE 11%, *Adv. Funct. Mater.*, 2021, **31**(14), DOI: **10.1002/adfm.202009996**.

38 J. Meiss, T. Menke, K. Leo, C. Uhrich, W. M. Gnehr, S. Sonntag, M. Pfeiffer and M. Riede, Highly efficient semitransparent tandem organic solar cells with complementary absorber materials, *Appl. Phys. Lett.*, 2011, **99**, 2009–2012, DOI: **10.1063/1.3610551**.

39 X. Li, R. Xia, K. Yan, J. Ren, H. L. Yip, C. Z. Li and H. Chen, Semitransparent Organic Solar Cells with Vivid Colors, *ACS Energy Lett.*, 2020, **5**, 3115–3123, DOI: **10.1021/acsenergylett.0c01554**.

40 Z. Hu, J. Wang, X. Ma, J. Gao, C. Xu, X. Wang, X. Zhang, Z. Wang and F. Zhang, Semitransparent organic solar cells exhibiting 13.02% efficiency and 20.2% average visible transmittance, *J. Mater. Chem. A*, 2021, **9**, 6797–6804, DOI: **10.1039/d1ta01135a**.

41 E. Pascual-San-José, G. Sadoughi, L. Lucera, M. Stella, E. Martínez-Ferrero, G. E. Morse, M. Campoy-Quiles and I. Burgués-Ceballos, Towards photovoltaic windows: Scalable fabrication of semitransparent modules based on non-fullerene acceptorsvialaser-patterning, *J. Mater. Chem. A*, 2020, **8**, 9882–9895, DOI: **10.1039/d0ta02994g**.

42 Z. Hu, J. Wang, X. Ma, J. Gao, C. Xu, K. Yang, Z. Wang, J. Zhang and F. Zhang, A critical review on semitransparent organic solar cells, *Nano Energy*, 2020, **78**, 105376, DOI: **10.1016/j.nanoen.2020.105376**.

43 Polysolar Limited (2021). PS-MC-ST Series panels.

44 Aleo Solar GmbH (2001). Aleo Solar PV Isolierglas Isolante.

45 Glaswerke Arnold GmbH & Co. KG (2011). VOLTARLUX ASI-Glas.

46 J. Park, K. Lee and K. Seo, 25-Cm^2 Glass-Like Transparent Crystalline Silicon Solar Cells With an Efficiency of 14.5%, *Cell Rep. Phys. Sci*, 2022, **3**, 100715, DOI: **10.1016/j.xcrp.2021.100715**.

47 C. Y. Tsai and C. Y. Tsai, See-through, light-through, and color modules for large-area tandem amorphous/microcrystalline silicon thin-film solar modules: Technology development and practical considerations for building-integrated photovoltaic applications, *Renew. Energy*, 2020, **145**, 2637–2646, DOI: **10.1016/j.renene.2019.08.029**.

48 S. Kuk, Z. Wang, H. Yu, C. Y. Nam, J. H. Jeong and D. Hwang, Nanosecond laser scribing for see-through CIGS thin film solar cells, *Prog. Photovoltaics*, 2019, 135–147, DOI: **10.1002/pip.3219**.

49 G. E. Eperon, V. M. Burlakov, A. Goriely and H. J. Snaith, Neutral color semitransparent microstructured perovskite solar cells, *ACS Nano*, 2014, **8**, 591–598, DOI: **10.1021/nn4052309**.

50 L. Rakocevic, R. Gehlhaar, M. Jaysankar, W. Song, T. Aernouts, H. Fledderus and J. Poortmans, Translucent, color-neutral and efficient perovskite thin film solar modules, *J. Mater. Chem. C*, 2018, **6**, 3034–3041, DOI: **10.1039/c7tc05863b**.

51 H. Eggers, S. Gharibzadeh, S. Koch, F. Schackmar, D. B. Ritzer, T. Abzieher, B. S. Richards, C. Erban and U. W. Paetzold, Perovskite Solar Cells with Vivid, Angle-Invariant and Customizable Inkjet Printed Colorization for Building-Integrated Photovoltaics, *Sol. RRL*, 2022, **6**(4), DOI: **10.1002/solr.202100897**.

52 K. Xiao, Y. H. Lin, M. Zhang, R. D. J. Oliver, X. Wang, Z. Liu, X. Luo, J. Li, D. Lai and H. Luo, *et al.*, Scalable processing for realizing 21.7%-efficient all-perovskite tandem solar modules, *Science*, 2022, **376**, 762–767, DOI: **10.1126/science.abn7696**.

53 H. Eggers, F. Schackmar, T. Abzieher, Q. Sun, U. Lemmer, Y. Vaynzof, B. S. Richards, G. Hernandez-Sosa and U. W. Paetzold, Inkjet-Printed Micrometer-Thick Perovskite Solar Cells with Large Columnar Grains, *Adv. Energy Mater.*, 2020, **10**(6), DOI: **10.1002/aenm.201903184**.

54 J. Li, J. Dagar, O. Shargaieva, M. A. Flatken, H. Köbler, M. Fenske, C. Schultz, B. Stegemann, J. Just, D. M. Többens, A. Abate, R. Munir and E. Unger, *et al.*, 20.8% Slot-Die Coated MAPbI3 Perovskite Solar Cells by Optimal DMSO-Content and Age of 2-ME Based Precursor Inks, *Adv. Energy Mater.*, 2021, **11**(10), DOI: **10.1002/aenm.202003460**.

55 L. Qiu, S. He, Z. Liu, L. K. Ono, D. Y. Son, Y. Liu, G. Tong and Y. Qi, Rapid hybrid chemical vapor deposition for efficient and hysteresis-free perovskite solar modules with an operation lifetime exceeding 800 hours, *J. Mater. Chem. A*, 2020, **8**, 23404–23412, DOI: **10.1039/d0ta09007g**.

56 M. A. Ruiz-Preciado, F. Gota, P. Fassl, I. M. Hossain, R. Singh, F. Laufer, F. Schackmar, T. Feeney, A. Farag and I. Allegro, *et al.*, Monolithic Two-Terminal Perovskite/CIS Tandem Solar Cells with Efficiency Approaching 25%, *ACS Energy Lett.*, 2022, **7**, 2273–2281, DOI: **10.1021/acsenergylett.2c00707**.

57 G. Westheimer, Visual acuity and hyperacuity, *Handbook of Optics*, 1975, pp. 570–572, DOI: **10.1097/00006324-198708000-00002**.

58 V. Saveljev, S.-K. Kim and J. Kim, Moiré effect in displays: a tutorial, *Opt. Eng.*, 2018, **57**, 1, DOI: **10.1117/1.oe.57.3.030803**.

59 C. Yang, D. Liu, M. Bates, M. C. Barr and R. R. Lunt, How to Accurately Report Transparent Solar Cells, *Joule*, 2019, **3**, 1803–1809, DOI: **10.1016/j.joule.2019.06.005**.

60 C. Yang, D. Liu, M. Bates, M. C. Barr and R. R. Lunt, Supplemental Information for How to Report Transparent Solar Cells, *Joule*, 2019, **3**(8), DOI: **10.1016/j.joule.2019.06.005**.

61 M. M. Giusti, R. E. Wrolstad and D. E. Smith, *Food Analysis Laboratory Manual*, 2017, pp. 219–224, DOI: **10.1007/978-3-319-44127-6**.

62 Berkeley Lab, US DOE, LBNL Windows and Daylighting Group, and National Fenestration Rating Council IGDB. Accessed: 2022/02/16.

63 J. Dou, Y. Bai and Q. Chen, Challenges of lead leakage in perovskite solar cells, *Mater. Chem. Front.*, 2022, **6**, 2779–2789, DOI: **10.1039/d2qm00632d**.

64 Y. Jiang, L. Qiu, E. J. Juarez-Perez, L. K. Ono, Z. Hu, Z. Liu, Z. Wu, L. Meng, Q. Wang and Y. Qi, Reduction of lead leakage from damaged lead halide perovskite solar modules using self-healing polymer-based encapsulation, *Nat. Energy*, 2019, **4**, 585–593, DOI: **10.1038/s41560-019-0406-2**.

65 Z. Li, X. Wu, S. Wu, D. Gao, H. Dong, F. Huang, X. Hu, A. K.-Y. Jen and Z. Zhu, An effective and economical encapsulation method for trapping lead leakage in rigid and flexible perovskite photovoltaics, *Nano Energy*, 2022, **93**, 106853, DOI: **10.1016/j.nanoen.2021.106853**.

66 S. Yang, S. Chen, E. Mosconi, Y. Fang, X. Xiao, C. Wang, Y. Zhou, Z. Yu, J. Zhao and Y. Gao, *et al.*, Stabilizing halide perovskite surfaces for solar cell operation with wide-bandgap lead oxysalts, *Science*, 2019, **365**, 473–478, DOI: **10.1126/science.aax3294**.

67 B. Niu, H. Wu, J. Yin, B. Wang, G. Wu, X. Kong, B. Yan, J. Yao, C. Z. Li and H. Chen, Mitigating the Lead Leakage of High-Performance Perovskite Solar Cells via in Situ Polymerized Networks, *ACS Energy Lett.*, 2021, **6**, 3443–3449, DOI: **10.1021/acsenergylett.1c01487**.

68 S. Chen, Y. Deng, X. Xiao, S. Xu, P. N. Rudd and J. Huang, Preventing lead leakage with built-in resin layers for sustainable

perovskite solar cells, *Nat. Sustain.*, 2021, **4**, 636–643, DOI: **10.1038/s41893-021-00701-x**.

69 D. B. Ritzer, T. Abzieher, A. Basibüyük, T. Feeney, F. Laufer, S. Ternes, B. S. Richards, S. Bergfeld and U. W. Paetzold, Upscaling of perovskite solar modules: The synergy of fully evaporated layer fabrication and all-laser-scribed interconnections, *Prog. Photovoltaics Res. Appl.*, 2022, **30**, 360–373.

70 B. A. Nejand, D. B. Ritzer, H. Hu, F. Schackmar, S. Moghadamzadeh, T. Feeney, R. Singh, F. Laufer, R. Schmager and R. Azmi, *et al.*, Scalable two-terminal all-perovskite tandem solar modules with a 19.1% efficiency, *Nat. Energy*, 2022, **7**, 620–630, DOI: **10.1038/s41560-022-01059-w**.

71 H. Booth, Laser processing in industrial solar module manufacturing, *J. Laser Micro Nanoeng*, 2010, **5**, 183–191, DOI: **10.2961/jlmn.2010.03.0001**.